Journal of Magnetism and Magnetic Materials 537 (2021) 168170

Contents lists available at ScienceDirect

Journal of Magnetism and Magnetic Materials

journal homepage: www.elsevier.com/locate/jmmm

Research articles

# Fast and universal approach for quantitative measurements of bistable hysteretic systems

Mohammad Reza Zamani Kouhpanji [a,b], P.B. Visscher [c], Bethanie J.H. Stadler [a,d,*]

[a] Department of Electrical and Computer Engineering, University of Minnesota-Twin Cities, Minneapolis 55455, USA
[b] Department of Biomedical Engineering, University of Minnesota-Twin Cities, Minneapolis 55455, USA
[c] Department of Physics and Astronomy, University of Alabama, Tuscaloosa Alabama, 35487-0234, USA
[d] Department of Chemical Engineering and Material Science, University of Minnesota-Twin Cities, Minneapolis 55455, USA

ARTICLE INFO

*Keywords:*
New, fast, and universal characterization
Projection method
Hysteretic systems
Hysteresis response

ABSTRACT

Accurate and fast characterization of hysteretic systems can accelerate progress in fields as diverse as biomedicine, sensors, data storage, and logic devices. Here, we introduce a fast approach to determine magnetic parameters (intrinsic coercivities of elementary domains, interaction fields between the domains, and the variances of both) of bistable hysteretic systems. The approach uses the first few points in first-order reversal curves (FORC) to mathematically and empirically determine the projections of traditional FORC diagrams onto the reversal field and applied field axes. Since this projection approach only requires a few points per each reversal curve (rather than 100+ points for 100+ curves compared to the traditional FORC method), the time of measurement is reduced by 50-100x over traditional FORC measurements. In addition, the projection results do not contain the typical FORC artifacts that have been disputed for decades. As a proof of concept, the projection analysis was used to determine the magnetic parameters of several arrays of bistable magnetic nanowires (MNWs), and the results were compared with the hysteresis loop and FORC results. For non-interacting arrays of MNWs, all three methods give the intrinsic coercivity with minor difference. While, the differences become significant for the interacting arrays of the MNWs that will be discussed in details.

## 1. Introduction

Hysteretic systems are ubiquitous in engineering, chemistry, biology, and even economics and social health. Hysteretic systems include magnetic nanostructures [1–5], living cells [6–12], piezoelectrics [13–15], ferroelectrics [16,17], piezoresistivity [18–21], thin-film transistors [22–26], and hydrogen adsorption metal-organics [27–29]. Fundamental to all of these systems is a need to understand the switching of elementary elements, or domains, and to control the entanglement between these domains. The traditional measurements for such systems are hysteresis loops, Fig. 1a, where the system response is measured while an appropriate stimulus is applied. For the examples above, response/stimulus pairs could be magnetization/magnetic field, mitosis/cycline, polarization/electric field, drain current/gate voltage, $H_2$ adsorption/$H_2$ flow, and optical or magnetic pumped/probed spins. The stimulus is swept from a saturating positive value to a saturating negative value and back. Unfortunately, hysteresis loops contain limited information because multiple phenomena affect the loop simultaneously. For example, interaction with neighboring domains may combine with the applied stimulus to cause a fraction of the domains to respond at lower or higher values than their intrinsic corresponding parameter. The resulting sheared hysteresis loop could be misinterpreted as the presence of inhomogeneous domains when it is in fact caused by the interaction between homogeneous domains, which is an extrinsic parameter.

To determine what intrinsic stimulus value is needed to switch each domain, what interactions exist between the domains, and the variances of both, several techniques have been developed with limited success. In materials science, scanning probe techniques, such as magnetic force microscopy (MFM) and scanning tunneling microscopy (STM) measure single domains while a uniform global field is applied. Modifications to transmission electron microscopy (TEM) have achieved remarkable measurements of individual domains as well. These techniques have high resolution, but they are inherently slow, two-dimensional at most, and involve a statistically small number of domains from which it is difficult to determine the full response of the system. A powerful

* Corresponding author at: Department of Electrical and Computer Engineering, University of Minnesota-Twin Cities, Minneapolis 55455, USA.
*E-mail address:* stadler@umn.edu (B.J.H. Stadler).

https://doi.org/10.1016/j.jmmm.2021.168170
Received 24 August 2020; Received in revised form 27 March 2021; Accepted 1 June 2021
Available online 10 June 2021

solution to overcome these limitations is to modify the macroscopic hysteretic characterization methods to achieve a fast characterization method while keeping the balance between accuracy and universality.

Among all advanced macroscopic approaches for characterizing the hysteretic properties, the first-order reversal curve (FORC) method stands up because it considers hysteretic systems composed of many microscopic as its fundamental building blocks, Fig. 1b. Briefly, Mayergoyz [30–32] proposed the current standard FORC measurement as an identification technique via the classical Preisach model [33], which describes magnetic hysteresis loops as a superposition of numerous independent relays, called hysterons. Hysterons represent the switching of single elementary particles with rectangular hysteresis loops, such as those of isolated MNWs acting like Stoner-Wohlfarth particles. Experimentally, FORC measurements begin by applying a large magnetic field (H) to ensure the positive saturation of a sample. Next, the H is reduced to a predefined field, known as the reversal field ($H_r$), and the moment of the sample is measured while H is retuned to positive saturation, see Fig. 1b. This process is repeated with decreasing $H_r$ to collect a family of magnetization curves, M(H, $H_r$), as a function of reversal field and applied field. The FORC distribution is defined as the second derivative of the magnetization with respect to the reversal field and applied field, as follows:

$$\rho = -\frac{1}{2}\frac{\partial^2 M(H,H_r)}{\partial H \partial H_r} \tag{1}$$

In FORC analysis, $\rho$ is plotted as a heat-map with the axes representing the coercive field (x-axis, $H_c = ½(H\text{-}H_r)$) and the interaction field (y-axis, $H_u = ½(H + H_r)$). Although the FORC technique is an exceptional method for the qualitative and sometimes quantitative explanation of complex systems [34–37], its data collection and analysis induce practical limitations that make is not favorable for both research laboratory and industrial development levels. First, its measurements are usually very time-consuming. The long measurements are usually contaminated with the moment and field drifts that produce spurious features that are mistakenly assigned to the magnetic properties of the hysteretic system. Second, its data analysis requires multiple derivatives and integrals that induce artifacts by amplifying the measurement noises [38–41]. What is worse, taking derivative with respect to the H (or $H_r$) causes to erase the features that they are solely a function of $H_r$ (or H) that causes to conceal real features.

In this paper, we use the FORC method as a backbone to establish a fast and universal approach for analyzing bistable hysteretic systems while suppressing the FORC method limitations. Note bistable hysteretic systems are those that their response can only have two states, either on (up) or off (down), such as 2D transistors (array of magnetic nanowires, MNWs). We first represent an analytical framework to illustrate the features of FORC heat-maps; and how they evolve the projection of the heat-maps on the $H_r$ and H axes. Then, we represent an experimental protocol to rapidly measure the projections on the $H_r$ and H axes followed by a theoretical model to extract the magnetic parameters, coercivity ($H_c$), interaction field ($H_u$), and their distributions. Next, we implement the projection method on several arrays of bistable MNWs as a proof of concept to find their magnetic parameters. Lastly, we compare the results from our measurement method, which is called the projection method, to the results from the FORC method and the hysteresis loop method to underpin their pros and cons.

## 2. Experimental protocol

As opposed to the traditional FORC method, the projection method focuses on the projection of the FORC heat-maps on the reversal field ($H_r$) and applied field (H) axes for describing the hysteresis behavior of bistable hysteretic systems. The FORC heat-maps are projected on the $H_r$ axis by taking an integral as follows

$$P_{H_r}(H_r) = \int_{H_r}^{\infty} \rho(H_r,H)dH = -\frac{1}{2}\frac{\partial M(H_r,H)}{\partial H_r}\bigg|_{H=\infty} + \frac{1}{2}\frac{\partial M(H_r,H)}{\partial H_r}\bigg|_{H=H_r} = 0 + \frac{1}{2}\frac{\partial M(H_r,H)}{\partial H_r}\bigg|_{H=H_r} \tag{2}$$

When the H is very large, the whole system is in the saturation state, therefore, the first term is zero because the magnetization no longer changes with $H_r$. The second term is the variation of the magnetization with respect of the $H_r$ at $H = H_r$, simply, it is the irreversible switching at $H_r$. Similarly, the FORC heat-maps are projected on the H axis as follows

$$P_H(H) = \int_{-\infty}^{H} \rho(H_r,H)dH_r = -\frac{1}{2}\frac{\partial M(H_r,H)}{\partial H}\bigg|_{H_r=H} + \frac{1}{2}\frac{\partial M(H_r,H)}{\partial H}\bigg|_{H_r=-\infty} = -\frac{1}{2}\frac{\partial M(H_r,H)}{\partial H}\bigg|_{H_r=H} + \frac{1}{2}\frac{\partial M_{lower}(H)}{\partial H} \tag{3}$$

Here, the first term determines the variation in the magnetization with respect to the H at $H = H_r$. This term is also known as the reversible switching at $H = H_r$ because it shows the spontaneous magnetization at this field. The second term shows the derivative of the lower branch of

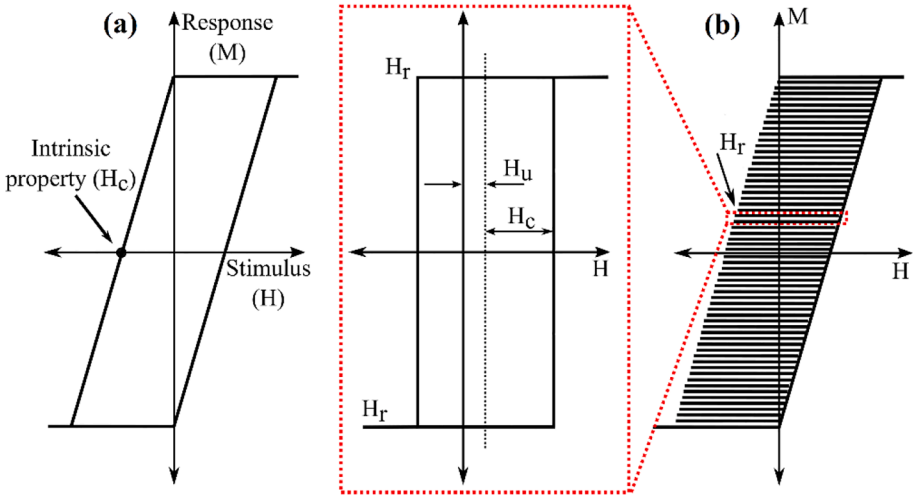


**Fig. 1.** Schematically illustrating the response/stimulus of hysteretic systems determined using, (a) the hysteresis loop measurement and (b) first-order reversal curve (FORC) measurement. Inset in subfigure (b) shows the response of a hysteron that switches as $H_r$, where the $H_c$ and $H_u$ are the intrinsic parameter (coercivity) and extrinsic parameter (interaction field), respectively.

the hysteresis loop ($M_{lower}$).

According to Eq. (2) and (3), both projections on the $H_r$ and H axes can be determined by measuring a few data points at the beginning of each FORC. It helps to significantly reduce the measurement time by collecting a few points instead of measuring several points for each FORC. Fig. 2 compares the FORC method with the projection method. The projection method protocol includes only measuring the first few data points for each FORC. However, it should be mentioned that the projection method measures the projections of the FORC heat-maps on the $H_r$ and H axes, not the coercivity ($H_c$) and interaction ($H_u$) axes. Therefore, it does not directly measures the $H_c$, $H_u$, and their distributions. In the next section, we propose a theoretical model for the projection method to find these values for bistable hysteretic systems.

## 3. Theoretical analysis

As mentioned in the previous section, the projection method measures the projections of the FORC heat-maps on the $H_r$ and H axes. To determine the coercivity ($H_c$), interaction fields ($H_u$), and their distributions for a hysteretic system, it is necessary to find the correlation between these parameters with results of the projection method. The simplest correlation can be achieved for bistable hysteretic systems, where the response has only two stable states, either on (up) or off (down). Therefore, we numerically model several bistable hysteretic systems with different levels of interaction and coercivity distributions to find the correlation between the simulation parameters and the features on the FORC heat-maps that determine the projections of the FORC heat-maps on the $H_r$ and H axes. Details about modeling are given in the SI. Fig. 3 shows the results of this analysis along with a scheme to illustrate how the important points are transformed on the $H_r$ and H axes.

The outer points are the most important because they determine the width of the projections on the $H_r$ and H axes, which can be readily determined from the projection method data. Other points collapse on each other during integration, e.g. all points along the dashed line in Fig. 3b. Therefore, we focus only on the outer points, here are labeled as A, B, and C. Our theoretical simulations of FORC heat-maps indicates that point A occurs where hysterons with minimum coercivity under the maximum interactions are found, ($H_c^{min}$, $H_u^{max}$). Point C indicates the hysterons with highest coercivity on the FORC heat-maps. They are the last hysterons to switch, that is, when the interaction field is maximum and opposing to their switching. Therefore, point C shows the hysterons that switch at fields equal to the maximum coercivity plus the maximum interaction, ($H_c^{max}$ + $H_u^{max}$, 0). Point B is the most mysterious point because we could not find an explicit relation between its location and the simulation parameters. Thus, we consider two unknown parameters to identify its location, ($H_c^B$, -$H_u^B$). Note these results also were realized in previous literature in simulations of FORC heat-maps of bistable arrays of MNWs and bistable magnetic dots [42–44].

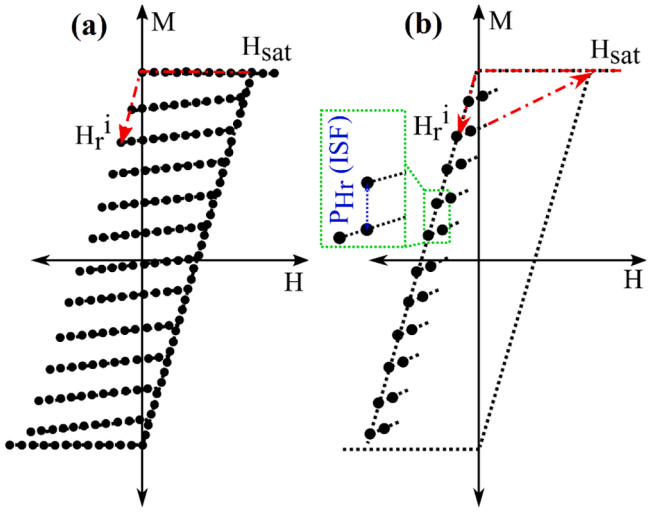


**Fig. 2.** Schematically compares the required data points for determining the magnetic parameters using (a) the first-order reversal curve (FORC) and (b) the projection method.

According to the FORC method, the correlation between the H and $H_r$ axes to the $H_c$ and $H_u$ axes are

$$H = \frac{1}{\sqrt{2}}(H_u + H_c) and H_r = \frac{1}{\sqrt{2}}(H_u - H_c) \tag{4}$$

It should be mentioned that the real relationship between the ($H_r$, H) plane and ($H_c$, $H_u$) plane is a 45 degrees rotation, which requires a factor of the square root of 2 instead of a factor of 2 as it is commonly used in the FORC formula [42]. Using Eq. (4), the location of the aforementioned points on $H_r$ and H axes will be as follows

On H axis On $H_r$ axis

$$A' = \frac{H_u^{max} + H_c^{min}}{\sqrt{2}} A'' = \frac{H_u^{max} - H_c^{min}}{\sqrt{2}} \tag{5a}$$

$$B' = \frac{-H_u^{B} + H_c^{B}}{\sqrt{2}} B'' = \frac{-H_u^{B} - H_c^{B}}{\sqrt{2}} \tag{5b}$$

$$C' = \frac{H_u^{max} + H_c^{max}}{\sqrt{2}} C'' = \frac{-H_u^{max} - H_c^{max}}{\sqrt{2}} \tag{5c}$$

According to Eq. (5) and Fig. 3, points A'' and C'' determine the width of the $P_{Hr}$ ($W_{Hr}$) and points B' and C' determine the width of $P_H$ ($W_H$). Note the $P_{Hr}$ and $P_H$ are the projection of the FORC heat-maps on the $H_r$ and H axes as defined in Eq. (2) and (3), respectively. That is because, for example, the $H_u^{max}$ + $H_c^{min}$ < $H_u^{max}$ + $H_c^{max}$ for projection onto the H axis. Therefore, one has

$$W_{Hr} = \frac{1}{\sqrt{2}}\left(2H_u^{max} + H_c^{max} - H_c^{min}\right) \tag{6a}$$

$$W_{H} = \frac{1}{\sqrt{2}}\left(H_u^{max} + H_c^{max} + H_u^{B} - H_c^{B}\right) \tag{6b}$$

For a better visualization, Fig. 3a provides the location of the points with exaggeration. One can use the terminology relationships to determine the width of $P_{Hr}$ and $P_H$ as follows:

$$W_{Hr} = |AB|cos(\beta_2) + |BC|sin(\eta_1) \tag{7a}$$

$$W_{Hr} = |AC|cos(\theta_1) \tag{7b}$$

$$W_{H} = |BC|cos(\eta_1) \tag{7c}$$

$$W_{H} = |AB|sin(\beta_2) + |AC|sin(\theta_1) \tag{7d}$$

According to Fig. 3a, the lengths and angles in Eq. (7) are

$$|AB| = \sqrt{\left(H_c^{B} - H_c^{min}\right)^2 + \left(H_u^{max} + H_u^{B}\right)^2} \tag{8a}$$

$$|AC| = \sqrt{\left(H_c^{max} + H_u^{max} - H_c^{min}\right)^2 + \left(H_u^{max}\right)^2} \tag{8b}$$

$$|BC| = \sqrt{\left(H_c^{max} + H_u^{max} - H_c^{B}\right)^2 + \left(H_u^{B}\right)^2} \tag{8c}$$

$$tan(\eta_2) = \frac{\Delta Y_{BC}}{\Delta X_{BC}} = \frac{H_u^{B}}{H_c^{max} + H_u^{max} - H_c^{B}} \qquad \eta_1 = \pi/4 - \eta_2 \tag{8d}$$

$$tan(\theta_2) = \frac{\Delta Y_{AC}}{\Delta X_{AC}} = \frac{H_u^{max}}{H_c^{max} + H_u^{max} - H_c^{min}} \qquad \theta_1 = \pi/4 - \theta_2 \tag{8e}$$

$$tan(\beta_1) = \frac{\Delta Y_{AB}}{\Delta X_{AB}} = \frac{H_u^{max} + H_u^{B}}{H_c^{B} - H_c^{min}} \qquad \beta_1 = \pi/4 + \beta_2 \tag{8f}$$

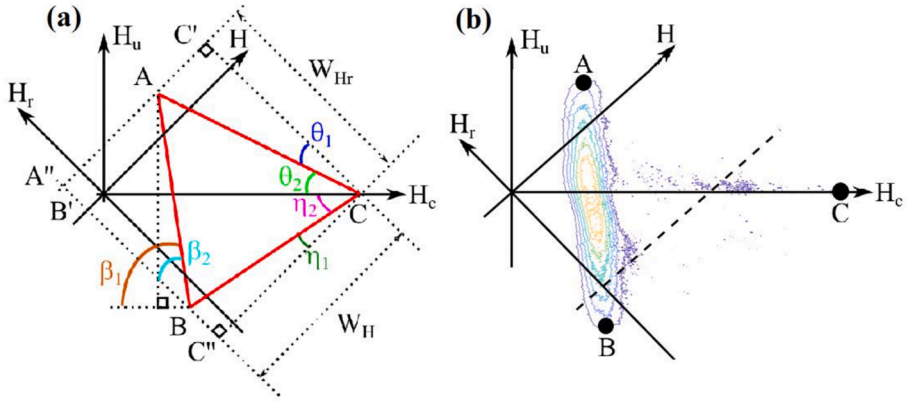


**Fig. 3.** a) Schematic of a FORC diagram showing the points of interest (A, B, and C) in the ($H_c$, $H_u$) plane and correlating the length of lines connecting the ($H_c$, $H_u$) plane onto ($H_r$, H) plane. b) Shows the theoretical simulation of a hysteretic system composed of bistable interacting hysterons with a Gaussian distribution of coercivity.

Substituting Eq. (6) and (8) into Eq. (7) provides four equations while there are five unknown parameters in Eq. (5) that must be calculated. Points A and C on the $H_r$ axis provide the last equation. Since one has points A and C locations on $H_r$ axis, their center is

$$Center of the W_{Hr} = \frac{[A'' on H_r axis] + [C'' on H_r axis]}{2} = -\frac{H_c^{max} + H_c^{min}}{2\sqrt{2}} = -\frac{H_c^{ave}}{\sqrt{2}} \tag{9}$$

Note, one could alternatively use the center of the $W_H$; however, since Eq. (6) gives a simpler relationship, we chose this one. Otherwise, there should not be any difference between the results if another is chosen.

Finding the magnetic parameters, $H_c$, $H_u$, and their distributions, requires solving Eq. (7) and Eq. (9) using conditions at Eq. (8). Since they are fully coupled and nonlinear, convergence to the right values is somehow troublesome. For simplicity, we first normalize them as follows and then solve them using a graphical approach. The normalization is

$$\xi = \frac{H_c^{min}}{H_c^{max} + H_u^{max}}\varphi = \frac{H_c^{B}}{H_c^{max} + H_u^{max}}\lambda = \frac{H_u^{B}}{H_c^{max} + H_u^{max}}\omega = \frac{H_u^{max}}{H_c^{max} + H_u^{max}} \tag{10}$$

Consequently, Eq. (6) to Eq. (8) will be

$$\frac{1}{\sqrt{2}}(1 + \omega - \xi) = \sqrt{(\varphi - \xi)^2 + (\omega + \lambda)^2}\cos(\beta_2) + \sqrt{(1 - \varphi)^2 + \lambda^2}\sin(\eta_1) \tag{11a}$$

$$\frac{1}{\sqrt{2}}(1 + \omega - \xi) = \sqrt{(1 - \xi)^2 + \omega^2}\cos(\theta_1) \tag{11b}$$

$$\frac{1}{\sqrt{2}}(1 + \lambda - \varphi) = \sqrt{(1 - \varphi)^2 + \lambda^2}\cos(\eta_1) \tag{11c}$$

$$\frac{1}{\sqrt{2}}(1 + \lambda - \varphi) = \sqrt{(\varphi - \xi)^2 + (\omega + \lambda)^2}\sin(\beta_2) + \sqrt{(1 - \xi)^2 + \omega^2}\sin(\theta_1) \tag{11d}$$

$$\tan(\beta_1) = \frac{\omega + \lambda}{\varphi - \xi} \tag{11e}$$

$$\tan(\theta_2) = \frac{\omega}{1 - \xi} \tag{11f}$$

$$\tan(\eta_2) = \frac{\lambda}{1 - \varphi} \tag{11g}$$

$$W_{Hr} = \frac{H_c^{max} + H_u^{max}}{\sqrt{2}}(1 + \omega - \xi) \tag{11h}$$

$$W_H = \frac{H_c^{max} + H_u^{max}}{\sqrt{2}}(1 + \lambda - \varphi) \tag{11i}$$

To graphically find the solutions for magnetic parameters, we consider two vectors for ω and λ, where each vector changes from 0 to 1. These two vectors form a 2D space and each point in this space can be substituted in Eq. (11-a) to (11-g) to find the solutions for ξ and φ in which these four equations are valid. Then, we use Eq. (11-h) and (11-i) constraints to identify all possible solutions leading to similar $H_u^{max}$ + $H_c^{max}$ values that meet the condition in Eq. (9), which gives the average coercivity ($H_c^{ave}$). If the same $H_c^{ave}$ were found, those values for ω, λ, φ, and ξ are the solutions. A typical issue for all graphical methods is that they sometimes result in multiple solutions or none. In these cases, one can consider tolerances indicating whether the solutions for $H_c^{ave}$ are identical or fall in an interval with a reasonable error. Choosing a large tolerance can cause very scattered results while a very tight tolerance may not result in a solution at all. Therefore, we first chose a moderate to large error tolerance to calculate the magnetic parameters. Then, we kept reducing the tolerance until a single (or a few) solutions were found. This was done very quickly (~10 s) using an automated algorithm written in MATLAB.

## 4. Experimental method

As a proof of concept, we electrodeposited different arrays of nickel (Ni) magnetic nanowires (MNWs) using a well-established electrodeposition technique inside nanoporous track-etched polycarbonate templates. Detailed information regarding the electrolyte and the electrodeposition conditions are given in the SI. To reach the bistable condition, we electrodeposited the MNWs with very large aspect ratios (length to radius) of at least 10, see the SEM images in the SI, to guarantee the bistable condition for each MNW array. We chose the Ni MNWs because they have negligible crystal anisotropy. Therefore, their coercivity is determined primarily by their shape anisotropy, e.g. the aspect ratio and diameter. X-ray diffraction data is presented in the SI to confirm the cubic structure of Ni. Note that the interaction fields can be adjusted using the templates' filling factor, defined as the ratio of the MNWs surface area to the total area of the template. In this study, four types of samples were synthesized with the following MNW diameters (array fill factors): 30 nm (0.5%), 50 nm (1%), 100 nm (2%), 200 nm (12%). The SEM images of the templates are given in the SI. The magnetic characteristics of the MNWs were measured using the hysteresis loop method, FORC method, and the projection method. Details

regarding the measurements are given in the SI. The hysteresis loop data and FORC data were analyzed according to the literature [44–46], and the projection data were analyzed as explained in the previous section.

## 5. Results and discussion

In Fig. 4, we plotted the results for the interaction field ($H_u$), coercivity ($H_c$), and their variances calculated using the hysteresis loop measurement, FORC measurement, and projection method. For a bistable hysteretic system, the $H_u$ distribution is a symmetric function centered at zero, where the number of on (up) and off (down) hysterons are the same. Therefore, it is sufficient to only determine its maximum value that is equal to its minimum value with a negative sign. The quantitative values for $H_u^{max}$, $H_c^{ave}$, and their variances according to the FORC measurement were calculated by projecting the FORC heat-maps on the $H_u$ and $H_c$ axes, respectively. Note that the hysteresis loop measurement is unable to determine the $H_u$ as well as the variances of the $H_u$ and $H_c$.

The main challenge of all magnetic characterization is decoupling the effects of the $H_u$ on the $H_c$ distribution. The presence of $H_u$ in hysteresis not only causes a shift in the $H_c$ distribution but also makes its distribution broaden, leading to a larger apparent coercivity variance ($\sigma_c$). Some literature considers this large variance to the contribution of the MNWs at the boundaries [42,43], or the geometrical non-uniformity [47–49], but this explanation was disputed later by experimental and theoretical analyses [37,42,50]. Furthermore, it was also observed using other magnetic measurements, such ferromagnetic resonance (FMR), that $H_u$ can cause large $\sigma_c$ if not fully decoupled from the $H_c$ distribution [51–55]. Here, the projection method validates this observation. According to Fig. 4a, as the MNWs diameter increases, the $H_c^{ave}$ decreases. Since the MNWs with diameters of 30 nm to 100 nm have negligible interactions compared to others (due to more distance between MNWs in these samples), all three methods provide the same $H_c^{ave}$. However, as the $H_u$ increases (with increasing the filling factor of the MNW arrays), Fig. 4b, there is a deviation between the results of the magnetic measurement methods, especially for the highly interacting MNWs array with a diameter of 200 nm. It should be emphasized, even though the FORC measurements scan the whole hysteresis loop area leading in a significantly slower measurements compared to the projection method, its results for the $H_c^{ave}$ are similar to the projection method. Specifically for interacting arrays of MNWs, the projection method and the FORC measurements predict similar $H_c^{ave}$, which are different than $H_c^{ave}$ from the hysteresis loop. This difference is due to the hysteresis loop's coupling of the interaction field effects on the $H_c$ distribution. Therefore, as can be seen in Fig. 4c, the hysteresis loop method also predicts very large values for the $\sigma_c$. The FORC method predicts a larger $\sigma_c$ than the projection method, but it is still significantly smaller than the hysteresis loop results. It is likely that the FORC method does not fully differentiate the $H_u$ effects from the $H_c$ variance, mainly due to the amplification of measurement noise (field and moment drifts) during the derivatives.

Another insight revealed by the projection method that reinforces this observation is the ratio of the $\sigma_c$ to the $H_c^{ave}$, Fig. 4d. The most likely reason for a variance in coercivity is a variance in MNW diameter within each sample. These effects have been studied broadly in the past, indicating that MNWs with larger diameters have smaller coercivity compared to MNWs with smaller diameters. Coercivity is dependent on the reversal mechanism which changes from coherent rotation of all spins [56–60] in small diameter nanowires to nucleation and propagation of a domain wall as the nanowire diameter increases [61]. Experimental and theoretical studies have shown that the nucleation and propagation of the domain walls occur at lower external fields as the diameter of MNWs increases, leading the coercivity to be proportional to the inverse of the diameter squared [62,63]. Furthermore, for bulk samples, $H_c$ becomes fairly independent of sample dimensions and is only proportional to the crystal anisotropy and exchange constant. Therefore, it is expected that the ratio of the $\sigma_c$ to $H_c^{ave}$ decreases as the diameter increases. Note the polycarbonate nanoporous templates were prepared in the same method leading to a similar standard deviation for the MNWs diameters for all samples, see the SEM images in the SI. The projection method renders compatible results with these facts, unlike the hysteresis loop and FORC results, see Fig. 4d. Indeed, the hysteresis loop shows a significant increase in the $\sigma_c$ to $H_c^{ave}$ ratio because it does not provide any information about $H_u$ and its effects on the $H_c$ distribution. Moreover, the FORC results also show a $\sigma_c$ to $H_c^{ave}$ ratio larger

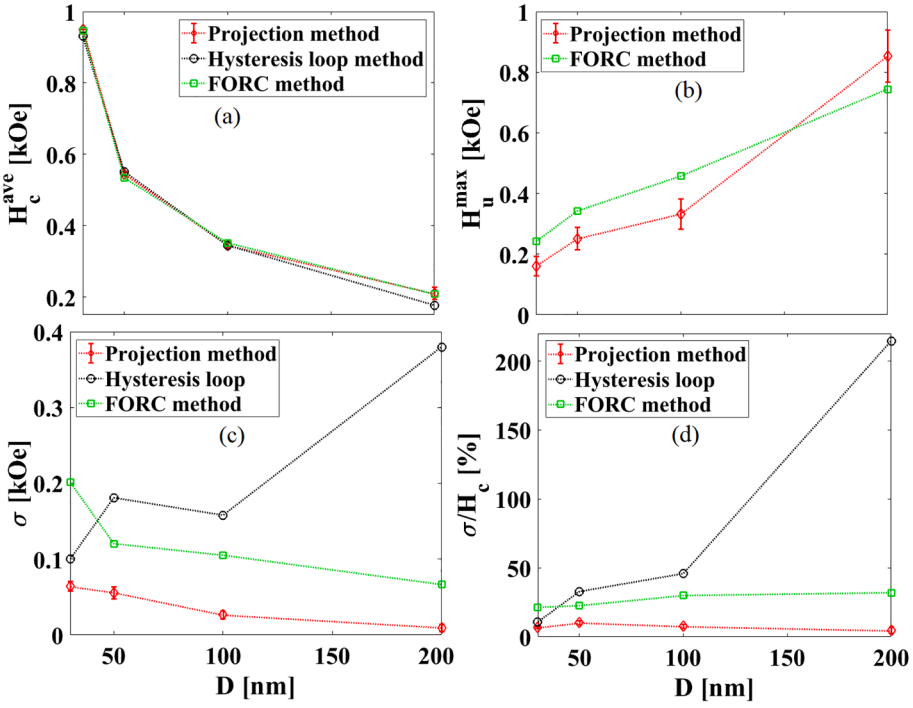


**Fig. 4.** Comparing the hysteretic parameters for the arrays of MNWs calculated using the hysteresis loop method, FORC method, and the projection method. Aside from subfigure (b), the error bars in other subfigures are in the same size as the symbols.

than the projection method, which we believe is a misrepresentation because the FORC method does not fully differentiate the $H_u$ effects from the $H_c$ distribution effects.

For all subfigures of Fig. 4, the error bars are within a reasonable range, it is in order of 25% for the worst case. There might be several sources for the errors which worth further studies in the future. The first source of uncertainties can be the location of the points A, B, and C that must be chosen from the $P_{Hr}$ and $P_H$ distributions. Since these are a single points that should be chosen, peaking different values can cause some variations in the final results. The second source of uncertainties can be number of the collected data points on each reversal curve. We indeed measured several different number of data points, N, (i.e. 4, 7, and 10), where we found that the N does not affect the results for the non-interacting MNW arrays while it could slightly affect the results for the interacting MNW arrays (data are shown in the SI). The last source of the uncertainties could also be due to the convergence of Eq. (11). In summary, being able to speed up the characterization of bistable magnetic systems by a factor of 50X-100X faster than FORC method without scarifying the accuracy would definitely benefit the magnetic community in all realms.

## 6. Conclusion

In summary, the projection method not only highly accelerates the measurements by a factor of 50X-100X but also fully differentiates the interaction fields from the coercivity distribution of bistable magnetic systems, which has been elusive for decades. Furthermore, the simple and unambiguous data acquisition and analysis of the projection method excel it to be readily adapted to analyze the hysteretic systems observed in physical sciences, social sciences, and biological sciences. Analyzing the magnetic parameters of magnetic nanowires (MNWs) array using the projection method is compatible with the previous theoretical and experimental analysis of these bistable hysteretic systems. Our comparative study of the hysteresis loop measurement, first-order reversal curve (FORC) measurement, and the projection method highlighted the significant effects of the interaction fields on the coercivity distributions, which could not be fully realized on highly interacting arrays of the MNWs using the hysteresis loop and FORC measurements. However, it should be mentioned that the provided data analysis here is valid only for bistable hysteretic systems, such as an array of the magnetic nanowires (MNWs) or perpendicular bit-patterned recording media that are measured along their uniaxial anisotropy (easy axis). For more complicated systems, where they violate the bistable condition, further theoretical simulation of the FORC must be included to determine an empirical defining the shape of their FORC heat-maps and the critical points for characterizing the magnetic parameters.

## 7. Data availability

The datasets presented in the manuscript and MATLAB program for processing the results are available from the corresponding author upon reasonable request.

## Author contributions

M.R.Z.K and B.J.H.S initiated the original idea and processed the data; M.R.Z.K conducted the experiments; M.R.Z.K, P.V, and B.J.H.S contributed to interpretation of the data and writing of the manuscript.

## Declaration of Competing Interest

The authors declare that they have no known competing financial interests or personal relationships that could have appeared to influence the work reported in this paper.

## Acknowledgment

This work is based upon work supported primarily by the National Science Foundation under grant no. CMMI-1762884. Portions of this work were conducted in the Minnesota Nano Center, which is supported by the National Science Foundation through the National Nano Coordinated Infrastructure Network (NNCI) under Award Number ECCS-1542202. Part of this work was performed at the Institute for Rock Magnetism (IRM) at the University of Minnesota. The IRM is a US National Multi-user Facility supported through the Instrumentation and Facilities program of the National Science Foundation, Earth Sciences Division (NSF/EAR 1642268), and by funding from the University of Minnesota. Parts of this work were also carried out in the Characterization Facility, University of Minnesota, which receives partial support from NSF through the MRSEC program.

## Appendix A. Supplementary data

Supplementary data to this article can be found online at https://doi.org/10.1016/j.jmmm.2021.168170.

## References

[1] M.R. Zamani Kouhpanji, B.J.H. Stadler, Projection method as a probe for multiplexing/demultiplexing of magnetically enriched biological tissues, RSC Adv. 10 (22) (2020) 13286–13292.
[2] M.R. Zamani Kouhpanji, J. Um, B.J.H. Stadler, Demultiplexing of Magnetic Nanowires with Overlapping Signatures for Tagged Biological Species, ACS Appl. Nano Mater. Mar. 3 (3) (2020) 3080–3087.
[3] M.R. Zamani Kouhpanji, A. Ghoreyshi, P.B. Visscher, B.J.H. Stadler, Facile decoding of quantitative signatures from magnetic nanowire arrays, Sci. Rep. 10 (1) (2020) 15482.
[4] M.R. Zamani Kouhpanji, B.J.H. Stadler, A Guideline for Effectively Synthesizing and Characterizing Magnetic Nanoparticles for Advancing Nanobiotechnology: A Review, Sensors 20 (9) (2020) 2554.
[5] M.R. Zamani Kouhpanji, B.J.H. Stadler, Magnetic nanowires for quantitative detection of biopolymers, AIP Adv. 10 (12) (2020) 125231.
[6] J.E. Ferrell, E.M. Machleder, The biochemical basis of an all-or-none cell fate switch in xenopus oocytes, Science 280 (805365) (1998) 895–898.
[7] X. Chen, F. Fu, Imperfect vaccine and hysteresis, Proc. R. Soc. B Biol. Sci. 286 (1894) 2019.
[8] S. Tripathi, H. Levine, M.K. Jolly, The Physics of Cellular Decision Making During Epithelial-Mesenchymal Transition, Annu. Rev. Biophys. 49 (1) (2020) 1–18.
[9] R.C. Stan, D.K. Bhatt, M.M. de Camargo, Cellular Adaptation Relies on Regulatory Proteins Having Episodic Memory: Proteins Modulate Cell Metabolism and Reproduction by Remembering, Transmitting, and Using Data on the Environment, BioEssays 42 (1) (2020) 1–7.
[10] J.R. Pomerening, E.D. Sontag, J.E. Ferrell, Building a cell cycle oscillator: Hysteresis and bistability in the activation of Cdc2, Nat. Cell Biol. 5 (4) (2003) 346–351.
[11] S. Mckenna, L. García-gutiérrez, D. Matallanas, D. Fey, BAX and SMAC Regulate Bistable Properties of the Apoptotic Caspase System, BioRxiv (2019) 1–50.
[12] Y. Jiang, et al., Single-Molecule Mechanistic Study of Enzyme Hysteresis, ACS Cent. Sci. 5 (10) (2019) 1691–1698.
[13] M.B. Ghasemian, T. Daeneke, Z. Shahrbabaki, J. Yang, K. Kalantar-Zadeh, Peculiar piezoelectricity of atomically thin planar structures, Nanoscale (2020) 2875–2901.
[14] B. Ducharne, B. Gupta, G. Litak, Simulation of synchronized-switching method energy harvester including accurate piezoceramic nonlinear behavior, Energies 12 (23) (2019) 1–12.
[15] D.K. Ngwashi, T.A. Mih, R.B.M. Cross, The influence of ZnO layer thickness on the performance and electrical bias stress instability in ZnO thin film transistors, Mater. Res. Express 7 (2020).
[16] Y. He, B. Bahr, M. Si, P. Ye, D. Weinstein, A tunable ferroelectric based unreleased RF resonator, Microsyst. Nanoeng. 6 (1) (Dec. 2020) 8.
[17] S. Mathews, R. Ramesh, T. Venkatesan, J. Benedetto, Ferroelectric field effect transistor based on epitaxial perovskite heterostructures, Science (80-.) 276 (5310) (1997) 238–240.
[18] L. Jin, et al., Microstructural origin of resistance-strain hysteresis in carbon nanotube thin film conductors, Proc. Natl. Acad. Sci. U.S.A 115 (9) (2018) 1986–1991.
[19] H. Mai, R. Mutlu, C. Tawk, G. Alici, V. Sencadas, Ultra-stretchable MWCNT–Ecoflex piezoresistive sensors for human motion detection applications, Compos. Sci. Technol. 173 (2019) 118–124.
[20] R. Tong, L. Cai, G. Chen, Rapid preparation of highly transparent piezoresistive balls for optoelectronic devices, R. Soc. Chem. Chem. Commun. 9 (2020).
[21] N.G. Apostol, et al., Resistance hysteresis correlated with synchrotron radiation surface studies in atomic sp 2 layers of carbon synthesized on ferroelectric (001) lead zirconate titanate in an ultrahigh vacuum, RSC Adv. 10 (3) (2020) 1522–1534.

[22] A.K. Ranade, R.D. Mahyavanshi, P. Desai, M. Kato, M. Tanemura, G. Kalita, Ultraviolet light induced electrical hysteresis effect in graphene-GaN heterojunction, Appl. Phys. Lett. 114 (15) (Apr. 2019), 151102.
[23] C. Lee, et al., Comparison of trapped charges and hysteresis behavior in hBN encapsulated single MoS 2 flake based field effect transistors on SiO 2 and hBN substrates, Nanotechnology 29 (33) (Aug. 2018), 335202.
[24] Y. Wang, et al., Direct observation of the hysteretic Fermi level modulation in monolayer MoS2 field effect transistors, Curr. Appl Phys. 20 (2) (Feb. 2020) 298–303.
[25] K.H. Han, G.-S. Kim, J. Park, S.-G. Kim, J.-H. Park, H.-Y. Yu, Reduction of Threshold Voltage Hysteresis of MoS 2 Transistors with 3-Aminopropyltriethoxy-silane Passivation and Its Application for Improved Synaptic Behavior, ACS Appl. Mater. Interfaces 11 (23) (Jun. 2019) 20949–20955.
[26] Y. Liu, P. Wang, Y. Wang, Y. Huang, X. Duan, Suppressed threshold voltage roll-off and ambipolar transport in multilayer transition metal dichalcogenide feed-back gate transistors, Nano Res. 13 (7) (Jul. 2020) 1943–1947.
[27] Y.-Z. Li, G.-D. Wang, H.-Y. Yang, L. Hou, Y.-Y. Wang, Z. Zhu, Novel cage-like MOF for gas separation, CO 2 conversion and selective adsorption of an organic dye, Inorg. Chem. Front. 2 (2020) 746–755.
[28] J. Hou, A.F. Sapnik, T.D. Bennett, Metal-organic framework gels and monoliths, Chem. Sci. 11 (2) (2020) 310–323.
[29] C.J. Zhang, K.T. Lian, G.Z. Huang, S. Bala, Z.P. Ni, M.L. Tong, Hysteretic four-step spin-crossover in a 3D Hofmann-type metal-organic framework with aromatic guest, Chem. Commun. 55 (74) (2019) 11033–11036.
[30] I.D. Mayergoyz, The classical Preisach model of hysteresis and reversibility, J. Appl. Phys. 69 (8) (1991) 4602–4604.
[31] I.D. Mayergoyz, Hysteresis models from the mathematical and control theory points of view, J. Appl. Phys. 57 (8) (1985) 3803–3805.
[32] I.D. Mayergoyz, Mathematical models of hysteresis (Invited), IEEE Trans. Magn. 22 (5) (1986) 603–608.
[33] F. Preisach, Uber die magnetische nachwirkung, Mitteilung aus dem Zentrallaboratorium des Wernerwerkes der Siemens Halske 277 (1935) 277–302.
[34] C.R. Pike, A.P. Roberts, K.L. Verosub, Characterizing interactions in fine magnetic particle systems using first order reversal curves, J. Appl. Phys. 85 (9) (1999) 6660–6667.
[35] M.K. Frampton, et al., First-order reversal curve of the magnetostructural phase transition in FeTe, Phys. Rev. B 214402 (95) (2017) 1–8.
[36] D.A. Gilbert, et al., "Probing the A 1 to L 10 transformation in FeCuPt using the first order reversal curve method, APL Mater. 2 (086106) (2014).
[37] S. Ruta, O. Hovorka, P.W. Huang, K. Wang, G. Ju, R. Chantrell, First order reversal curves and intrinsic parameter determination for magnetic materials; Limitations of hysteron-based approaches in correlated systems, Sci. Rep. 7 (February) (2017) 1–12.
[38] R.J. Harrison, J.M. Feinberg, FORCinel: An improved algorithm for calculating first-order reversal curve distributions using locally weighted regression smoothing, Geochem. Geophys. Geosyst. 9 (5) (2008).
[39] D. Cimpoesu, I. Dumitru, A. Stancu, DoFORC tool for calculating first-order reversal curve diagrams of noisy scattered data, J. Appl. Phys. 125 (2) (2019).
[40] F. Groß, et al., gFORC: A graphics processing unit accelerated first-order reversal-curve calculator, J. Appl. Phys. 126 (16) (Oct. 2019), 163901.
[41] T.A. Berndt, L. Chang, "Waiting for Forcot: Accelerating FORC Processing 100× Using a Fast-Fourier-Transform Algorithm", *Geochemistry*, Geophys. Geosystems 20 (12) (Dec. 2019) 6223–6233.
[42] C.-I. Dobrotă, A. Stancu, What does a first-order reversal curve diagram really mean? A study case: Array of ferromagnetic nanowires, J. Appl. Phys. 113 (4) (Jan. 2013), 043928.
[43] C.-I. Dobrotă, A. Stancu, Tracking the individual magnetic wires' switchings in ferromagnetic nanowire arrays using the first-order reversal curves (FORC) diagram method, Phys. B Condens. Matter 457 (Jan. 2015) 280–286.
[44] D.A. Gilbert, et al., Quantitative decoding of interactions in tunable nanomagnet arrays using first order reversal curves, Sci. Rep. 4 (2014) 1–5.
[45] B.F. Valcu, D.A. Gilbert, K. Liu, S. Technology, Fingerprinting Inhomogeneities in Recording Media Using the First-Order Reversal Curve Method, IEEE Trans. Magn. 47 (10) (2011) 2988–2991.
[46] J.G. Fernández, V.V. Martínez, A. Thomas, V.M. de la Prida Pidal, K. Nielsch, Two-step magnetization reversal FORC fingerprint of coupled bi-segmented Ni/Co magnetic nanowire arrays, Nanomaterials 8 (7) (2018) 1–15.
[47] A. Rotaru, et al., Interactions and reversal-field memory in complex magnetic nanowire arrays, Phys. Rev. B 134431 (84) (2011) 1–9.
[48] F. Béron, et al., Magnetic Behavior of Ni / Cu Multilayer Nanowire Arrays Studied by First-Order Reversal Curve Diagrams, IEEE Trans. Magn. 44 (11) (2008) 2745–2748.
[49] F. Beron, L. Clime, M. Ciureanu, D. Menard, R.W. Cochrane, A. Yelon, Reversible and quasireversible information in first-order reversal curve diagrams, J. Appl. Phys. 101 (2007).
[50] F. Beron, L. Clime, M. Ciureanu, D. Menard, R.W. Cochrane, A. Yelon, Magnetostatic interactions and coercivities of ferromagnetic soft nanowires in uniform length arrays, J. Nanosci. Nanotechnol. 8 (2008) 2944–2954.
[51] C. Moya, Ó. Iglesias, X. Batlle, A. Labarta, Quantification of Dipolar Interactions in Fe3-xO4 Nanoparticles, J. Phys. Chem. C 119 (42) (2015) 24142–24148.
[52] J. De La Torre Medina, L. Piraux, J.M. Olais Govea, A. Encinas, Double ferromagnetic resonance and configuration-dependent dipolar coupling in unsaturated arrays of bistable magnetic nanowires, Phys. Rev. B - Condens. Matter Mater. Phys. 81 (14) (2010) 1–11.
[53] A. Encinas-Oropesa, M. Demand, L. Piraux, I. Huynen, U. Ebels, Dipolar interactions in arrays of nickel nanowires studied by ferromagnetic resonance, Phys. Rev. B - Condens. Matter Mater. Phys. 63 (10) (2001) 1044151–1044156.
[54] M.R. Zamani Kouhpanji, B.J.H. Stadler, Unlocking the decoding of unknown magnetic nanobarcode signatures, Nanoscale Adv. 3 (2) (2021) 584–592.
[55] M.R. Zamani Kouhpanji, B.J.H. Stadler, Beyond the qualitative description of complex magnetic nanoparticle arrays using FORC measurement, Nano Express 1 (1) (2020) 010017.
[56] L.G. Vivas, et al., Magnetic anisotropy in CoNi nanowire arrays: Analytical calculations and experiments, Phys. Rev. B 85 (3) (Jan. 2012), 035439.
[57] J. Escrig, et al., Geometry dependence of coercivity in Ni nanowire arrays, Nanotechnology 19 (7) (2008).
[58] D.H. Qin, Y. Peng, L. Cao, H.L. Li, A study of magnetic properties: FexCo1-x alloy nanowire arrays, Chem. Phys. Lett. 374 (5–6) (2003) 661–666.
[59] C. Bran, A.P. Espejo, E.M. Palmero, J. Escrig, M. Vázquez, Angular dependence of coercivity with temperature in Co-based nanowires, J. Magn. Magn. Mater. 396 (Dec. 2015) 327–332.
[60] R. Lavín, et al., Angular dependence of magnetic properties in Ni nanowire arrays Angular dependence of magnetic properties in Ni nanowire arrays, J. Appl. Phys. 103903 (2009) (2014) 1–6.
[61] A. Aharoni, A. Aharoni, Magnetization in a prolate spheroid," vol. 1118, no. 1986, 2014.
[62] L.G. Vivas, On the magnetic and structural properties of Co and Co-based nanowire arrays, 2012.
[63] M.R. Zamani Kouhpanji, B. Stadler, Magnetic Nanowires toward Authentication, Part. Part. Syst. Charact. 38 (2) (2021) 2000227.